Proceedings of Global Power and Propulsion Society
ISSN-Nr: 2504-4400
GPPS Hong Kong 2023
October 17-19, 2023
www.gpps.global

GPPS-TC-2023-0272

AEROELASTIC ASSESSMENT OF THE SECOND FLEXURE MODE EXCITATION IN A LOW PRESSURE RATIO FAN

Atsushi Tateishi
IHI Corporation
tateishi7871@ihi-g.com
Akishima-shi, Tokyo, Japan

Mizuho Aotsuka
IHI Corporation
aotsuka9957@ihi-g.com
Akishima-shi, Tokyo, Japan

Shinya Kusuda
IHI Corporation
kusuda5841@ihi-g.com
Akishima-shi, Tokyo, Japan

Nozomi Tanaka
IHI Corporation
tanaka1257@ihi-g.com
Mizuho-machi, Tokyo, Japan

Tomonori Enoki
IHI Corporation
enoki3133@ihi-g.com
Akishima-shi, Tokyo, Japan

Takeshi Murooka
IHI Corporation
murooka3906@ihi-g.com
Akishima-shi, Tokyo, Japan

ABSTRACT

During the development of high by-pass aircraft engine fans, stall flutter often becomes a major issue because it restricts their part-speed operability at near-stall conditions. Stall flutter is usually experienced on the first flexure mode, where a few nodal diameters are dominant. However, our recent tests showed strong non-synchronous excitation for the second flexure (2F) mode containing multiple nodal diameters, which is a distinguishing characteristic from well-known stall flutter. This paper aims to understand the mechanism of the observed 2F excitation. Aerodynamic damping is evaluated by nonlinear transient CFD simulations across a range of fan massflow near stall. The aerodynamic damping turns negative when vortex shedding near the blade tip spills upstream and interacts with the leading edge of the neighbouring blade. Also, the vortex shedding behaviour and resulting aerodynamic damping clearly depend on the blade amplitude. The vortex shedding has broadband spectra for both frequency and circumferential modes under low amplitude, and they lock on the blades' motion under large amplitude. From these observations, it is concluded that the observed 2F excitation can be categorized into non-synchronous vibrations found in recent literature. The coincidence of blade vibration and vortex shedding is also discussed from unsteady signal processing.

INTRODUCTION

In order to meet the requirement for reducing fuel burn of commercial aircraft engines, it has been important to achieve their higher overall efficiency and lower weight together. The overall efficiency of the engine can be gained by increasing propulsive efficiency, which can be realised by lowering exhaust jet velocity. Therefore, future aircraft engine fans are expected to have higher by-pass ratio and lower pressure ratio. This trend brings engine manufacturers new aerodynamic and structural design spaces. At the same time, it has been a potential fear that new aeromechanical phenomena emerge and restrict their operating ranges.

Flutter is an aeromechanical instability found in axial flow turbomachinery, which must be addressed during the development of aircraft engine fans. It is caused by the negative aerodynamic damping due to the coupling of blades' vibration and motion-excited aerodynamic force, and generally occurs near the blades' structural frequency, which is generally non-integer-multiples of the shaft speed (i.e., non-synchronous). For modern wide-chord fan blades, flutter often occurs in the stall-side of the fan operating map and restricts their operating range. This often becomes critical in part-speed conditions where the flutter boundary becomes closer to the engine work line on the ground.

Another blade vibration called Non-Synchronous Vibration (NSV) have been intensively studied so far in the front stages of compressors (Kielb et al., 2003, Espinal et al., 2018) and recently in Low Pressure Ratio (LPR) fans (Rodrigues et al., 2021). Although the terminology NSV contains some ambiguity because flutter is also categorized into "non-synchronous" vibration, in the context of turbomachinery aeromechanics, NSV often incorporates with specific flow unsteadiness like flow separation (Sanders, 2005), tip clearance flow (Drolet et al., 2013) or acoustic resonance (Fiquet et al., 2022).

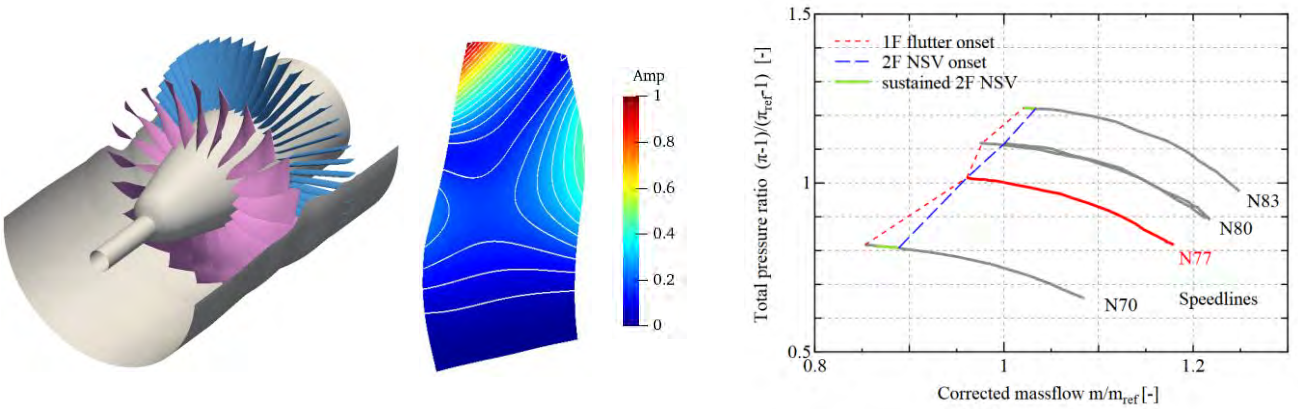

(a) Rig overview **(b) 2F modeshape** **(c) 1F flutter and 2F NSV regions**

Figure 1. IHI LPR fan test rig and stability limit

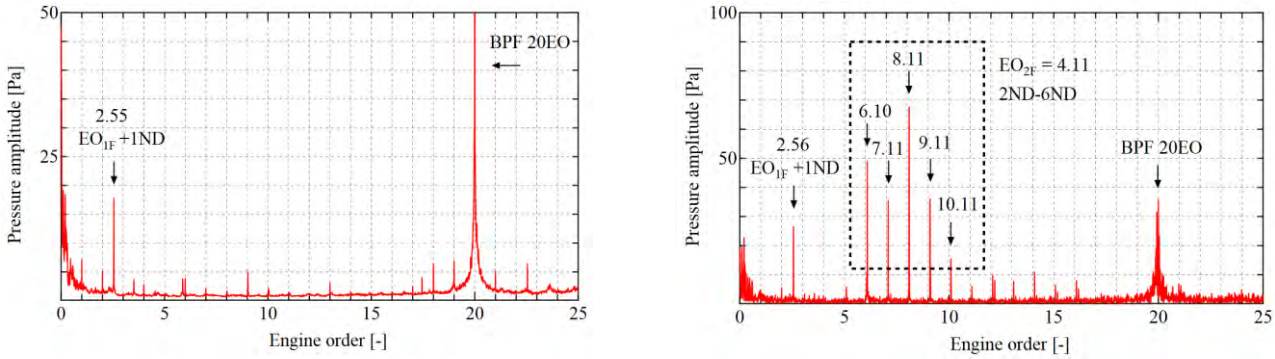

(a) 1F-ND1 Flutter (N80 speed) **(b) 2F NSV (N77 speed)**

Figure 2. Difference in unsteady pressure signals between 1F flutter and 2F NSV

During rig tests, NSV pronounces coherent signals of blades' vibration and pressure disturbance, like flutter. Flutter and NSV is sometimes hard to distinguish however, recent detailed experimental studies have revealed that NSV incorporates with the convective vortex shedding near the tip region, and the vortex shedding locked into the frequency and spatial pattern of the blades' deflection and impinged to the neighbouring blades (Brandstetter et al., 2018). Based on this observation, a new analytical model for NSV is proposed by Stapelfeldt and Brandstetter (2020). They successfully reproduced the lock-in phenomenon by the developed model, and concluded that the NSV with vortex shedding is convection-dominant. Also, a new terminology "convective NSV" is proposed to distinguish it from other types of NSV.

Under such recent progress in the NSV researches, IHI also have experienced strong second flexure (2F) mode vibration near stall conditions during rig tests of a LPR fan. Because few reports exist for fan flutter in the 2F mode and the signals during vibration has somewhat different characteristics than well-known fan stall flutter, the authors have begun to suspect that the 2F vibration is close to NSV under separated flow near stall. This 2F mode vibration is the main focus in this paper and referred to as "2F NSV" hereafter for simplicity.

The objective of this paper is to assess the excitation mechanism of the observed 2F NSV by unsteady flow near stall using detailed aeromechanical simulations. After highlighting the difference of 1F flutter and 2F NSV observed in our rig tests, numerical methods are briefly explained. In order to quantify the flow structure during blade vibration, post processing technique by time-space Fourier transformation is specially developed. The time evolution of aerodynamic damping and unsteady flow structure are carefully evaluated by transient simulations with different blade amplitude. Finally the mechanism of the present 2F NSV and possible coincidence of unsteady flow and blade vibration are discussed.

EXCITATION OF 2F MODE IN A LPR FAN RIG

The case studied in this paper is an IHI LPR fan test rig, which is specially developed for aeroelastic assessments in future high by-pass engine fans. Figure 1 summarizes the overview of the rig and stability limits experienced during tests. The fan shown in Fig. 1 (a) has 20 rotor blades and 48 exit guide vanes, which is mounted on the test facility in Japan Aerospace eXploration Agency (JAXA). The fan is connected with a plenum chamber upstream and a scroll exhaust downstream. The overview of the test facility and our past related work is reported by Hayashi et al. (2019).

The rotor is manufactured as a blisk made of titanium alloy. The disk is designed to be stiff enough, therefore the structural coupling between the blades are negligible. Also, the mistuning level identified by the standard deviation of

natural frequency is below 0.5% for both 1F and 2F modes. This level is sufficiently small and the flutter onset point is expected to be almost unchanged according to our past flutter evaluation (Tateishi et al., 2016). Figure 1 (b) shows the 2F modeshape expected on the 77% shaft speed. The nodal line exists from the midspan of the leading edge toward the tip trailing edge. The highest displacement exists at the tip leading edge.

Figure 1 (c) summarizes the excitation onset and stress limit points observed in the test. Both the first flexure (1F) flutter and 2F NSV were observed on four speedlines from N77 to N83. The onset points indicates where the vibratory stress level suddenly increased, while the all speed lines ends when the stress reaches the pre-set limits for safety. It can be seen that the 2F NSV tends to arise prior to the 1F flutter. On the N70 and N83 speedlines, the 2F NSV was moderate enough to continue the test. On the other hand, on the N77 and N80 speedlines, the 2F excitation was strong enough to immediately stop the test. On the N77 speedline the 2F NSV occurred at the same time with the 1F flutter. For N80 speedlines, different stability limits were obtained from different runs. In the first and second tests, 1F and 2F excitations occurred respectively, where the onset point of 2F NSV had higher massflow than the 1F onset. From these data, it can be said that the 2F NSV can limit the fan operability severer than the 1F flutter.

The difference between the 1F flutter and 2F NSV can be seen from the spectra of unsteady pressure during excitation which is shown in Fig. 2. These spectra are observed by a flash-mounted unsteady pressure transducer on the shroud located at approximately one axial chord upstream from the rotor leading edge. Because of the distance between the blade and transducer, it is anticipated that the pressure signal is mainly form composed of the acoustic wave generated by the blades' motion. The blades' vibration is monitored by both strain gauges and tip-timing system however, it is not presented in detail for clarity.

On the stationary frame of reference, the frequency of pressure fluctuation generated by the rotor vibration can be obtained as follows, considering the frequency shift due to the change of reference frame and circumferential vibration pattern (i.e., nodal diameter).

$$\mathrm{EO}_{\mathrm{abs}} = \mathrm{EO}_{\mathrm{rot}} + \mathrm{ND} \tag{1}$$

Two results are presented for N80 and N77 speedlines, where the structural frequencies for 1F and 2F modes are 1.55 and 4.11, respectively. The response during 1F excitation in Fig. 2 (a), only the peak of 2.55EO is significant, which is generated by 1F-ND1 Forward Traveling Wave (FTW). On the other hand, the response during 2F NSV shows multiple peaks from 6.10 to 10.11EO with the interval of 1EO, which means that multiple FTWs from ND2 to ND6 are simultaneously excited. Among these NDs, the highest peak at 8.11EO corresponding to ND4 is thought to be the primal component of the 2F N

SV. This significant excitation of multiple NDs is one of notable differences which distinguishes the 2F NSV from 1F flutter with a few dominant low nodal diameters. At the same time, the difference poses several questions on 2F NSV.

1. The relationship with "convective NSV" involved with the vortex shedding?
2. How we can evaluate the onset and characteristics of excitation?
3. What is the underlying phenomenon which excites multiple nodal diameters at the same time?

In order to answer these questions, detailed aeromechanics simulations are conducted.

METHODOLOGIES

Target speedline and blade vibration patterns

The N77 speedline in Fig. 1 (c) is chosen as a target case in this paper, because the 2F onset point was close to the work line and the stress level at the onset was high enough to immediately stop the test. According to literature, the unsteady flow pattern like vortex shedding can be affected by the blade vibration amplitude. Furthermore, the frequency and spatial pattern of unsteady flow can synchronize with the blades' vibration pattern under large blade amplitude (i.e., lock-in).

Therefore, the change in flow phenomenon and possibility of excitation are assessed by obtaining aerodynamic damping over wide range of blade amplitude. The interaction between the blade motion and unsteady flow is considered by one-way manner, where the blade motion (e.g., frequency, nodal diameter, modeshape, and amplitude) is kept constant during the simulations. The targeted blade vibration pattern is ND4, which was thought to be the primal component of the observed 2F NSV, because the frequency of the highest pressure amplitude during NSV corresponds to ND4 according to Fig. 2(b). Three test cases are prepared with maximum 2F mode amplitude of 0.3%c, 1.2%c, and 4.8%c. The blades' structural frequency is 4.3EO, which is obtained from the FEM analysis result. Here, the 0.3%c and 4.8%c amplitudes correspond to a typical value for flutter simulations and the pre-set limit for the 2F mode response in the rig test (i.e., scope limit), respectively. Therefore, the 4.8%c amplitude represents the maximum blade amplitude experienced in the rig test.

Numerical method and aerodynamic damping evaluation

The CFD code UPACS Vibrate, originally developed by JAXA (Yamane et al., 2001), is employed for the present simulations. It is based on three-dimensional Unsteady Reynolds Averaged Navier-Stokes (URANS) equations with arbitrary Lagrangian-Eulerian formulation. The equations are discretized by the finite volume method on multi-block

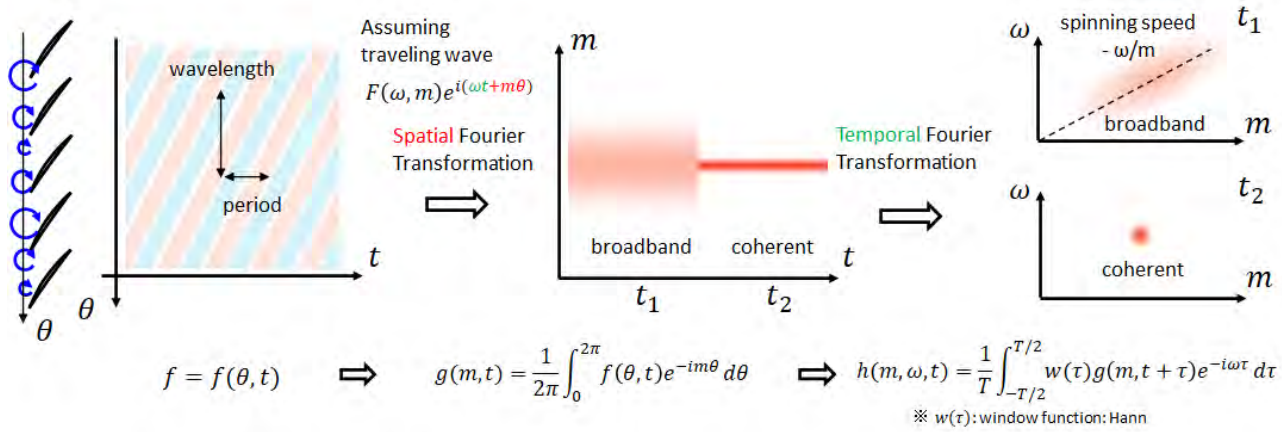

Figure 3. Space-time Fourier transformation of unsteady signals

structured grids. The blades' motion are explicitly applied by the moving grid module. The Spalart-Allmaras one-equation model is employed to estimate the eddy viscosity. Similar numerical setups have been successfully applied for our flutter (Aotsuka and Murooka, 2014) and forced response evaluations (Aotsuka et al, 2012).

The aerodynamic damping is evaluated by the work-per-cycle principle. When the aerodynamic damping turns from positive into negative, the blades' vibration becomes unstable and its amplitude grows exponentially. The structural modeshape is extracted from the FEM analysis result, and mapped onto the CFD grid. Under harmonic prescribed motion of the blade surface, the aerodynamic work and resulting aerodynamic damping can be obtained as follows.

$$W_{\mathrm{cyc}} = \int_{t=0}^{T}\iint_{S} -(p\boldsymbol{n}\cdot\boldsymbol{v})dS\,dt \quad , \quad \zeta_{\mathrm{aero}} = -\frac{W_{\mathrm{cyc}}}{2\pi\omega^2 q_0^2} \tag{2}$$

Here, ω and q_0 are the angular frequency and modal amplitude of the prescribed blade motion, respectively. These are determined from the structural frequency and modeshape of the 2F mode obtained by prior FEM structural analysis.

Data processing for unsteady flowfield

In order to assess the frequency and spatial pattern of the unsteady flow which will arise at near-stall conditions, the space-time Fourier transformation is applied to the unsteady signal sampled during unsteady simulations. Figure 3 illustrates the strategy of data sampling and processing in this study. The unsteady sampling is done along a circumferential line θ where the relevant unsteady flow may exist. Extracting the fluctuation component by subtracting time-averaged value for each sampling point, the time-space plot can be obtained like the leftside of Fig.3. The time period and circumferential wavelength can be roughly estimated by the time-space diagram.

Then, for each sampling time, the Fourier transformation is applied in the circumferential direction. This operation analyses the components of sinusoidal spatial modes existing at each time instance. Plotting the amplitude of each circumferential mode number m along with time t, the time-mode diagram is obtained like the centre of Fig. 3. When the signal has multiple closely separated modes, the diagram looks dispersed like around the time t_1. Contrary, when only single mode dominates the fluctuation, strong single peak appears like around t_2.

Finally, in order to identify the frequency ω for each mode, the time-domain Fourier transformation is applied over the timespan of interest T. Here, the Hann window is multiplied to enforce the periodicity of signal in time. The expected mode-frequency diagrams are shown in the right side of Fig. 3. From the dispersed modes around t_1, each mode has its own frequency, and it may spread around the plane. The coherent signal around t_2 may be the coherent signal in time too, resulting single spot in the mode-frequency plane. After two Fourier transformations, the spinning speed of the circumferential mode, Ω_{spin}, can be obtained from the frequency ω and mode number m as follows. This spinning speed is useful to discuss the underlying flow phenomenon and chance of interaction with blade vibration. Please note that all these operations are conducted on the rotating frame of reference.

$$\Omega_{\mathrm{spin}} = -\frac{\omega}{m} \tag{3}$$

Settings for unsteady simulation and data sampling

The computational model is a full-annulus configuration shown in Fig. 1 (a). The number of grid points for the rotor and stator are 2.21 and 1.06 million per passage respectively, yielding 93 million points in total. This size is determined by preliminary grid study. The time steps per one blade oscillation is 2200, corresponds to 9460 steps per shaft revolution.

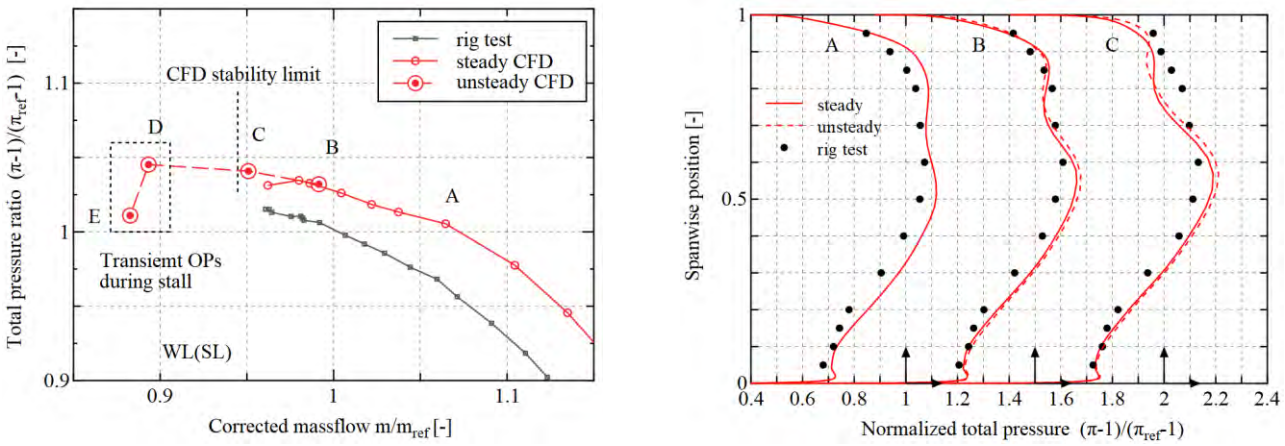

(a) 77% speedline **(b) Spanwise total pressure distributions**

Figure 4. Steady aerodynamic performance and validation with experimental data

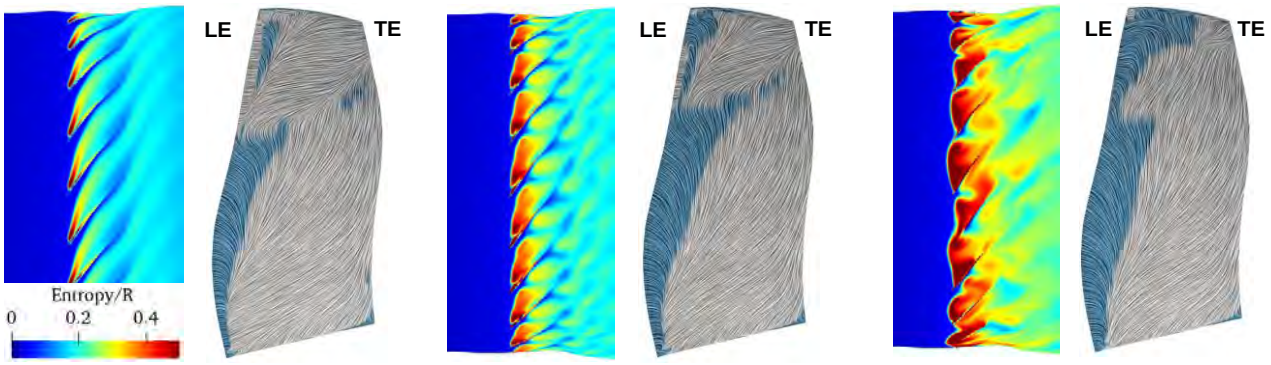

(a) OP B **(b) OP C** **(c) OP D**

Figure 5. Flow structures toward stall. Left: entropy contour at 98% span. Right: streamline on the blade suction surface, with axially reversed flow area indicated by dark blue.

The sampling station used for the discussion is located at 95% span height, $10\%c_x$ downstream from the rotor trailing edge. The number of sampling points in the circumferential direction is 720, resulting to the pitch of 0.5 degrees and 36 points in a blade-to-blade passage. The sampling frequency is 110 per one 2F oscillation and approximately 480 per shaft revolution, resulting the Nyquist frequency of 240EO, which is well above the range of interest. The frequency resolution in time-domain Fourier transformation is approximately 0.36EO, obtained from the timespan of 12 cycles of 2F oscillation.

RESULTS AND DISCUSSION

Flow characteristics without blade vibration

Before the aeroelastic assessment, the fan aerodynamic characteristics are obtained without blade vibration and compared with corresponding rig test results. Both steady and unsteady simulations are conducted in order to identify the operating point where the flow unsteadiness appears.

Figure 4 shows the comparisons of rotor speedlines (a) and spanwise distributions of normalized total pressure at the leading edge of FEGV (b). The rig test data are evaluated from time-averaged total temperature and total pressure measured by the Kiel probe heads instrumented on the leading edges of the fan exit guide vanes, while the numerical results are obtained from the mass flow average of the instantaneous flow fields. The operating conditions are labelled as A to E, as the massflow decreases. The simulations slightly overpredicts the total pressure rise however, the global trend well agrees with the rig test. The stability limit in the experiment corresponds to the onset point of 2F NSV. On the other hand, in the CFD results, the stability limit is determined by the last converged point with gradually increasing outlet static pressure. The steady simulation fails to converge near the rig stability limit of $m/m_{\mathrm{ref}} = 0.96$. The unsteady simulation stably converges until OP C, whose massflow of $m/m_{\mathrm{ref}} = 0.95$. The operating points D and E are unstable ones and plotted from the instantaneous data during stall.

From Fig. 4 (b), it can be seen that the total pressure near shroud significantly increased in the test between the OP B and C. This behaviour is qualitatively appeared in the simulations. The difference between steady and unsteady simulations

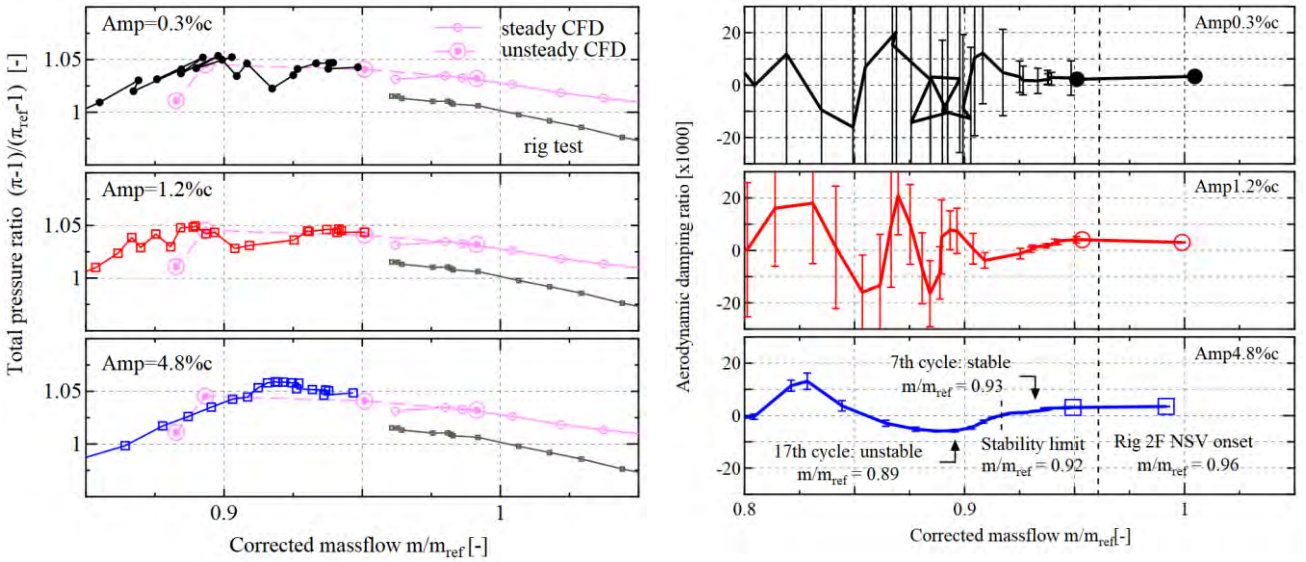

(a) Operating conditions **(b) Aerodynamic damping**

Figure 6. Time histories in transient simulations evaluated for each oscillation cycles

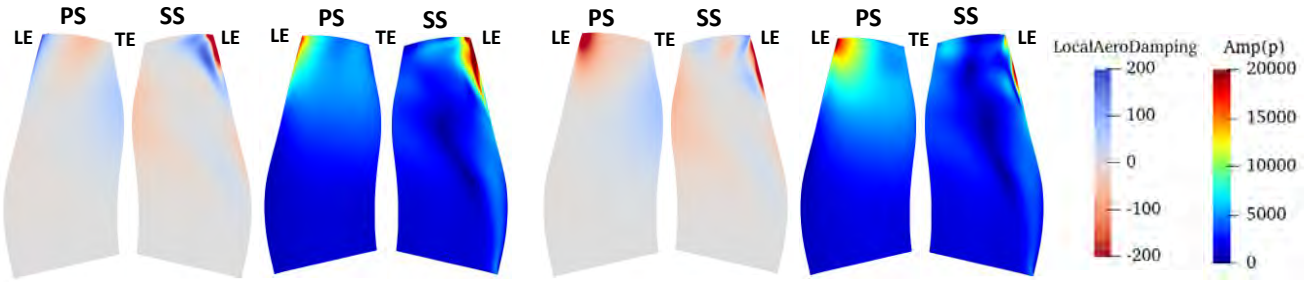

(a) 6th cycle (positive damping) **(b) 17th cycle (negative damping)**

Figure 7. Local aerodynamic damping (left) and unsteady pressure amplitude (right) for 2F-ND4 (amp=4.8%c)

can also be observed, especially for the OP C. The distribution from unsteady simulation shows more wiggled pattern over 80% span height, which implies the difference of flow behaviour between steady and unsteady results near the shroud.

The difference in the flow patterns near the shroud the blade surface are compared in Fig. 5. These results are from unsteady simulations. The entropy contour is used to show the flow pattern near shroud. Also, axially reversed flow area is indicated by dark blue region on the blade surface. The flow structure near the tip is significantly different among the operating points. On the OP B, high entropy area starts near the leading edge and travels toward downstream. This high entropy area is originated both from tip clearance flow and radially migrated separated flow on the blade suction side, which can be confirmed from the streamline on the blade surface.

This high entropy area looks stable on OP B however, it becomes unstable and forms shedding-like discrete patterns near the tip on OP C. Also, it is seen from the blade surface streamline that the axially-reversed area exists on the leading edge near the shroud. The flow instability further develops as the operating point moves from OP C to OP D. Comparing Fig. 5 (c) with (b), it is observed that the high-entropy region starts impinging to the neighbouring blades during stall. Corresponding snapshot of the streamline on the suction side shows that the flow is separated and axially reversed at the leading edge for all span height, and the separated flow accumulated near the tip. This growth of separation can be the factor for the change of unsteadiness near the shroud.

Aerodynamic damping evaluation: transient simulation toward stall

The aerodynamic damping of the 2F mode is evaluated for three different amplitude. In order to identify the relationship between the unsteady flow and aerodynamic damping characteristics, it would be necessary to evaluate at least on three operating conditions shown in Fig. 5. However, our preliminary evaluation showed that the aerodynamic damping for 2F-ND4 was positive until OP C. Also, during the evaluation of aerodynamic damping, the flow could not converge into time-periodic state on OP D, because this was an unstable condition during stall. Therefore, transient simulations are planned to evaluate the aerodynamic damping from OP C. The simulations are initiated from OP C by rising the outlet

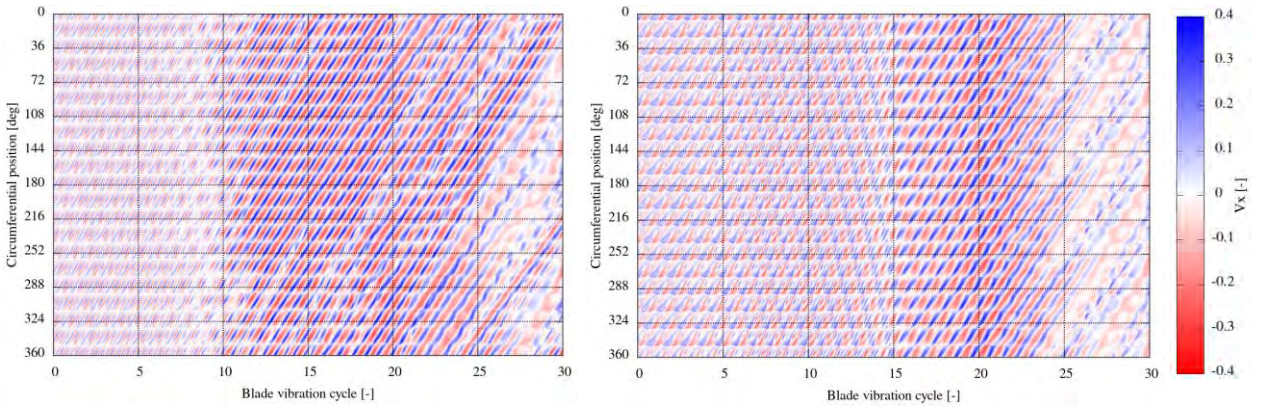

(a) time-space diagaram, amp = 1.2%c **(b) time-space diagaram, amp = 4.8%c**

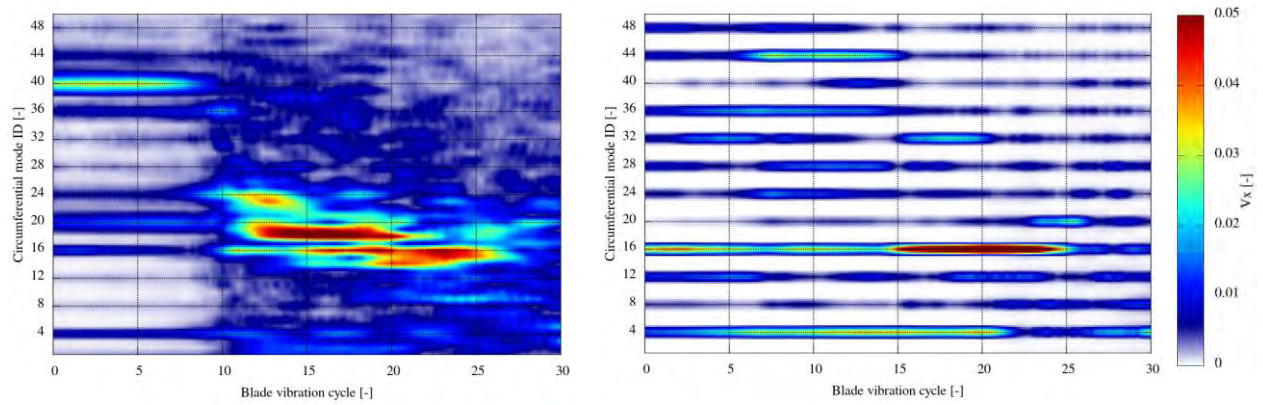

(c) circumferential modes, amp = 1.2%c **(d) circumferential modes, amp = 4.8%c**

Figure 8. Evolution of flow unsteadiness (axial velocity, 10%Cx from TE at 95% span)

static pressure by 0.5% to initiate stall. The instantaneous operating points and aerodynamic damping over each blade oscillation cycle are monitored during the transient simulations.

Figure 6 (a) shows the history of operating points and for three blade amplitudes: 0.3%c, 1.2%c, and 4.8%c. The symbols in transient results indicate the operating points of each blade oscillation. The massflow decreases as time advances, and therefore the operating condition moves from right to left on the characteristic map. All the transient results qualitatively agree with the speedline without blade vibration, shown by the pink lines.

Figure 6 (b) summarizes the history of aerodynamic damping, which is evaluated for each blade oscillation cycles. Large symbols represent the results of the stable operating points, and the transient results are shown by the vertical bars. Again, the massflow decreases as time passes. The width of bars indicates the standard deviation of aerodynamic damping evaluated for each blade, which means the circumferential variation of aerodynamic damping. For lower amplitude cases of 0.3%c and 1.2%c, it can be seen that the 2F-ND4 becomes unstable as the massflow decreases, but the mean damping frequently switches between the positive and negative values, and the variation of damping is very high. On the other hand, the largest amplitude case of 4.8%, the variation of aerodynamic damping is significantly smaller than the other two cases. In addition, the range of massflow which shows negative damping can be clearly identified. From these results, it can be anticipated that the interaction of unsteady flow and blade vibration changes as the blade amplitude increases.

For the largest amplitude of 4.8%, the instability onset massflow is slightly under-predicted (rig 2F onset: $m/m_{\mathrm{ref}} = 0.96$, CFD: $m/m_{\mathrm{ref}} = 0.92$). Although this difference is still high, in the authors' view it is sufficiently encouraging that the 2F aeroelastic instability can be confirmed in numerical simulations. Using this result, the de-stabilizing mechanism are discussed hereafter.

Figure 7 presents local aerodynamic damping and unsteady pressure amplitude synchronizes with 2F-ND4. Here, the aerodynamic damping for the 6$^{\mathrm{th}}$ and 17$^{\mathrm{th}}$ cycles are positive and negative, respectively. By comparing the local aerodynamic damping between the 6$^{\mathrm{th}}$ cycle (a) and 17$^{\mathrm{th}}$ cycle (b), it can be clearly seen that the leading edge of the pressure side turns from positive to strong negative damping. At the same time, the unsteady pressure amplitude significantly increases where the damping contribution turns negative. This position corresponds where the high-entropy fluid start to interact with the neighbouring blade, as discussed in Fig. 5 (b) and (c). Therefore, the instability of 2F-ND4 is expected to be closely related to the well-developed unsteady flow near the shroud.

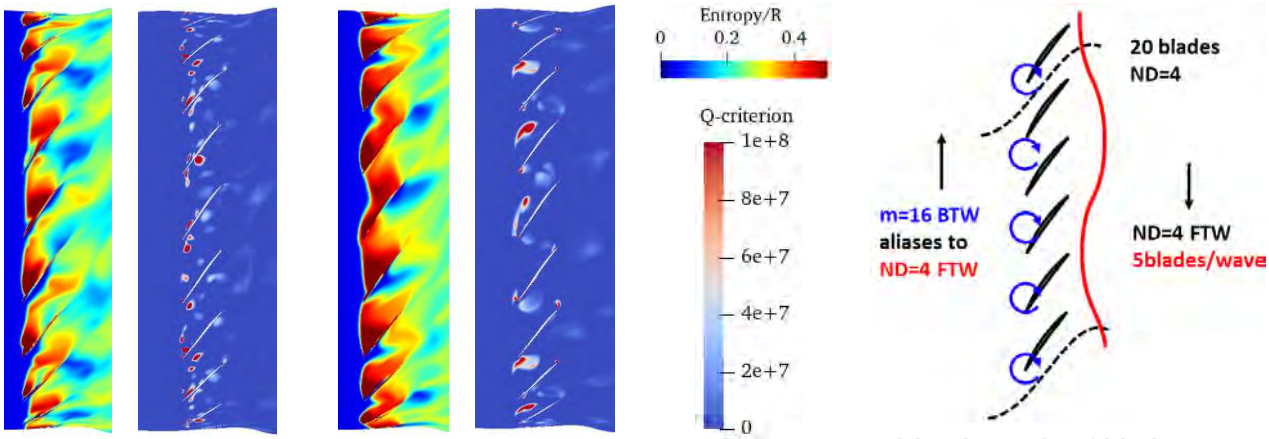

(a) 6th cycle (positive damping) (b) 17th cycle (negative damping) (c) schematic of blade-vortex interaction

Figure 9. Vortex shedding near the tip (amp = 4.8%c)

Unsteady flow patterns and relation with blade excitation

In order to confirm the consistency of the unsteady flow pattern and the resulting excited nodal diameter, the time development of circumferential modes are analysed by the space-time diagram and time-mode diagram, as explained in Fig. 3. Figure 8 shows the time-space and resulting time-mode diagrams obtained from the 2F amplitudes of 1.2 and 4.8%. Axial velocity is chosen to evaluate the flow instability, because its variation corresponds to flow disturbances due to vortex shedding.

The effect of blade amplitude can be clearly seen by comparing the 1.2%c and 4.8%c cases. In the time-space diagram of the 1.2% amplitude case in Fig. 8 (a), relatively large-scale fluctuation emerges from around the 10th blade cycles. Then the size of pattern gradually becomes larger until 20th cycles, and suddenly grows again around the 25th cycles. The fluctuation pattern is not completely uniform in the circumferential direction. The flow fluctuation in 1.2%c contains multiple circumferential modes as presented in Fig. 8 (c). From the 0th to 10th cycles, the mode number of 40 is dominant. Then, after the 10th cycle, the modes from 12 to 24 are suddenly appeared. These lower modes corresponds to the change in flow pattern in Fig. 5 (b) and (c).

In the largest amplitude case of 4.8%c, the qualitative aspect of the arising circumferential modes is significantly different from the 1.2%c case, as expected from the trend in aerodynamic damping. The time-space diagram Fig. 8 (b) shows much organized pattern than the 1.2%c case. According to the circumferential modes shown in Fig. 8 (d), only the multiples of 4, which is the prescribed nodal diameter in the simulation, have high amplitude. This result means that the spatial pattern of unsteady flow is determined by the blade vibration. In the lower blade amplitude cases the unsteady flow behaves naturally, and therefore closely-separated multiple circumferential modes arise due to the non-uniformity in the flowfield. On the other hand, under sufficiently large blade amplitude, the unsteady flow synchronizes the blade vibration and only specific circumferential modes arise. This finding is consistent with the prior work of Zhao et al. (2020).

In Fig. 8 (d), it can also be seen that the dominant circumferential modes are changing during the transient simulation. At the beginning of simulation the mode number of 16 has relatively high amplitude. This mode 16 is thought to be appeared by the scattering of prescribed ND4 oscillation by the 20 rotor blades (20-4=16). From the time 5-15 cycles, the high mode number of 44 is appeared, and then from the 15th cycles the amplitude of mode number of 16 is suddenly increased. This timing of dominant mode shift corresponds to when the aerodynamic damping switches into negative. Therefore, it is expected that the energization of mode 16 leads the destabilization of 2F-ND4 oscillation shown in Fig. 7.

In order to further confirm the local unsteady flow pattern and the destabilizing mechanism, the vortex shedding pattern is compared between the stable and unstable cycles in Fig. 9 (a) and (b). The vortex cores are identified by the positive part of Q-criterion, which corresponds the red part in the Q-criterion contour. During the stable 6th cycle, small scale vortex cores can be observed in Fig. 9 (a). This small scale vortices may correspond to the 44th mode found in Fig. 8 (d). On the unstable 17th cycle in Fig. 9 (b)., the size of vortices is much larger than that in the 6th cycle. Four vortex cores are exist inside 5 blade pitches, therefore this vortex shedding clearly corresponds to the mode 16 in full annulus of 20 blade pitches.

The interaction of vortex shedding and blades are schematically illustrated in Fig. 9 (c). There are 16 vortices traveling backward in the circumferential direction. The blade vibration pattern excited by the mode 16 backward traveling wave is ND4 forward traveling, because of the aliasing effect. From this relationship, it can be confirmed that the impingement of vortices is the root cause of the destabilizing effect of the pressure side leading edge shown in Fig. 7. This mechanism agrees well with that of convective NSV (Stapelfeldt, S. and Brandstetter, C., 2020).

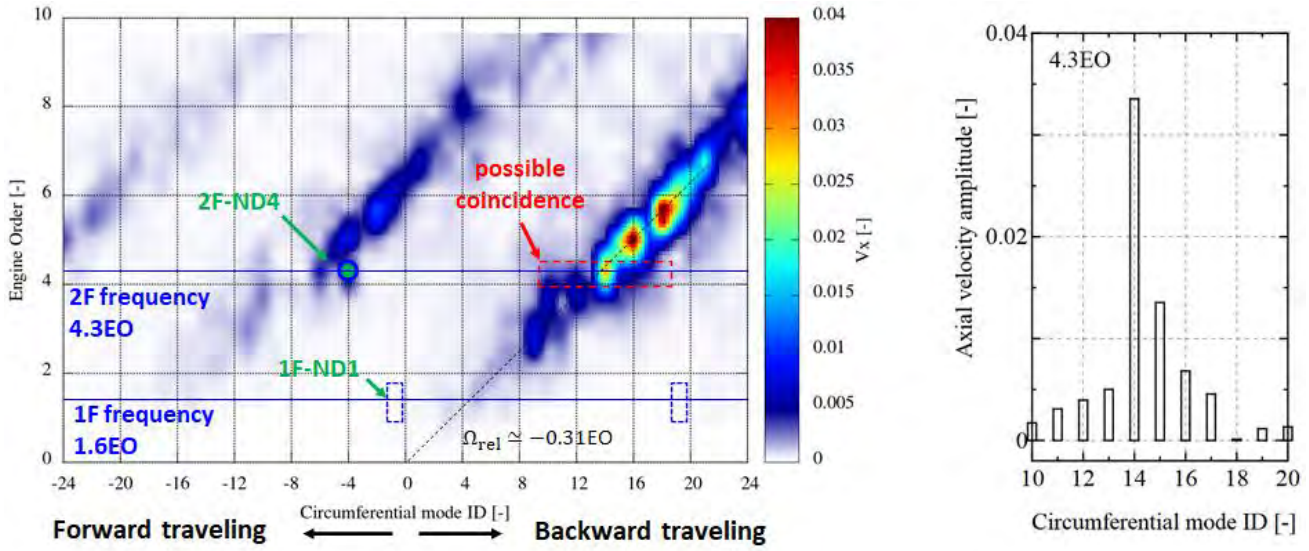

(a) Time-space Fourier transformation result **(b) Closeup for 4.3EO**

Figure 10. Assessment of coincidence due to vortex shedding (amp = 1.2%c, time-space DFT from 14-26 2F cycles)

Quantitative evaluation of unsteady flow: time-space spectra and coincidence with vortex shedding

For the largest amplitude of 4.8%c the vortex shedding completely locks into the blade vibration. On the other hand, for the smaller amplitude of 1.2%c, the vortex shedding occurs naturally. By analysing the unsteady flow pattern, the range of possible coincidence can be evaluated. Figure 10 shows the result of time-space Fourier transformation in the 1.2%c blade amplitude case. The timespan used is 14-26 2F oscillation cycles, where multiple circumferential modes exist according to Fig. 8 (c). Figure 10 (a) shows the mode-frequency diagram. Large amplitude due to vortex shedding can be observed in the modes from 8 to 20, whose frequency varies from 3 to 8 EO.

In the convective NSV, the excitation frequency due to vortex shedding is directly correlated with the convective speed of vortices (Stapelfeldt and Brandstetter, 2020). In the present result, $\Omega_{\mathrm{rel}} = -\omega/m = -0.31$EO approximately covers the high amplitude modes from 8 to 24, which is shown by the dark dotted line in Fig. 10 (a). The convective speed estimated from 2F NSV in the experiment was approximately -0.26EO and about 16% lower than the CFD. According to the experimental work by Brandstetter et al. (2018), the convective speed changes about 10% across the NSV onset. Unfortunately the convective speed could not directly obtained from our rig test due to the limitation in instrumentation. Such data would be quite useful for validating the NSV simulation from the unsteady aerodynamics viewpoint.

The frequency depends on the modes, and therefore coincidence occurs when the flow frequency eventually matches with the structural frequency. Figure 10 (b) shows the closeup around high amplitude region for the 2F mode of 4.3EO. Here, modes of 14-16 are relatively higher than the other modes, which can excite forward traveling waves of ND4-6 through alias. The vortex shedding contains multiple circumferential modes and can excite multiple nodal diameters, which can be the reason for the existence of multiple nodal diameter in the 2F NSV observed in the rig test.

The above discussion for coincidence can also be made for the 1F-ND1 flutter occurred in the rig test. If the 1F-ND1 excitation is convective NSV due to vortex shedding, the excitation source should be exist around the mode 19, which aliases to ND1. From Fig. 10 (a), there is no significant component on the 1F frequency of 1.6EO around the mode 19. Therefore, contrary to the 2F NSV, it is estimated that 1F flutter was not directly excited by the vortex shedding coherent with the blade vibration.

CONCLUSION

Detailed aeromechanical simulations were conducted in order to assess the excitation mechanism of the 2F mode near stall. The aerodynamic damping and unsteady flow structures were evaluated over a range of operating conditions, where the vortex shedding pattern significantly changed during the transient simulations. The conclusions are summarized as follows.

1. The 2F excitation found in the rig test can be explained by the coincidence of vortex shedding and the interaction with the 2F mode. When the blade amplitude is low, the vortex shedding naturally occurs at its own aerodynamic frequency and contains multiple circumferential modes. These vortices can excite multiple nodal diameters simultaneously, which supports the experimental observation.

2. As the blade vibration amplitude increases, the vortex shedding becomes locked into the blade vibration. Under this lock-in condition, the aerodynamic circumferential modes becomes significantly limited with the given structural nodal diameter.
3. The aerodynamic damping for ND4 FTW turns negative when the shed vortices near the shroud spill upstream of the blades and impinge to the leading edge of the neighbouring blades. The dominant circumferential mode in the vortex shedding is 16 BTW and it excites ND4 by aliasing with 20 rotor blades.
4. The 2F vibration observed in the test is categorized into convective NSV because of the existence of vortex shedding as an excitation source. Contrary, it is estimated that the 1F flutter in the test was not directly excited by the vortex shedding coherent with the blade vibration.

Although the evaluated 2F NSV onset point has slightly lower massflow however, the present observation qualitatively agrees with the experiment. Toward accurate prediction, the onset point and state of vortex shedding should be predicted accurately. The prediction of such complex turbulent flow would be a challenging area in turbomachinery CFD. Also, both detailed aerodynamic and aeroelastic measurement data are needed for validation purposes.

ACKNOWLEDGEMENT

The authors acknowledge JAXA for providing access to UPACS Vibrate CFD code.

NOMENCLATURE

π	total pressure ratio
ω	angular frequency
m	circumferential mode number
$\boldsymbol{n}$	blade surface normal vector
p	static pressure
Q	Q-criterion
q_0	modal amplitude
S	blade surface area
t	time
W_{cvc}	aerodynamic work per one blade oscillation
ζ_{aero}	aerodynamic damping ratio

Subscript

$_{\mathrm{abs}}$	Absolute frame of reference
$_{\mathrm{ref}}$	Reference values

Abbreviation

1F	First Flexure
2F	Second Flexure
BTW	Backward Traveling Wave
CFD	Computational Fluid Dynamics
FEM	Finite Element Method
FTW	Forward Traveling Wave
EO	Engine Order
LPR	Low Pressure Ratio
ND	Nodal Diameter
NSV	Non Synchronous Vibration
OP	Operating Point

REFERENCES

Aotsuka, M., Kato, D., and Murooka, T. (2012). Numerical Analysis of Forced Response of High Pressure Compressor Cascade. ISUAAAT13-S2-3. Proceedings of the 13th International Symposium on Unsteady Aerodynamics, Aeroacoustics and Aeroelasticity of Turbomachines.

Aotsuka, M. and Murooka, T. (2014). Numerical Analysis of Fan Transonic Stall Flutter. ASME Paper GT2014-26703. https://doi.org/10.1115/GT2014-26703

Hayashi, R., Tanaka, N., Enoki, T., Murooka, T., Kato, D., Masaki, D., Kazawa, J., Enomoto, S., and Nishizawa, T. (2019). Experimental Study of Laminar Flow Effect for Transonic Engine Fan. IGTC-2019-088. Proceedings of the International Gas Turbine Congress 2019 Tokyo.

Brandstetter, C., Jungst, M., and Schiffer, H-P. (2018). Measurements of Radial Vortices, Spill Forward, and Vortex Breakdown in a Transonic Compressor. J. Turbomach 140(6), 061004. https://doi.org/10.1115/1.4039053

Drolet, M., Vo, H, D., and Mureithi, N, W. (2013). Effect of Tip Clearance on the Prediction of Nonsynchronous Vibrations in Axial Compressors. J. Turbomach 135(1), 011023. https://doi.org/10.1115/1.4006401

Espinal, D., Im, H-S., and Zha, G-C. (2018), Full-Annulus Simulation of Nonsynchronous Blade Vibration Excitation of an Axial Compressor. J. Turbomach 140(3), 031008. https://doi.org/10.1115/1.4038337

Fiquet, A-L., Aubert, S., Buffaz, N., Vercoutter, A., and Brandstetter, C. (2022). Trapped Acoustic Modes in an Axial Multi-Stage Compressor Leading to Non-Synchronous Blade Vibrations. Int. J. Turbomach. Propuls. Power 7, 6. https://doi.org/10.3390/ijtpp7010006

Kielb, R. E., Barter, J. W., Thomas, J. P., and Hall. K. C. (2003). Blade Excitation by Aerodynamic Instabilities -A Compressor Blade Study. ASME Paper GT2003-38634. https://doi.org/10.1115/GT2003-38634

Rodrigues, M., Soulat, L., Paoletti, B., Ottavy, X., and Brandstetter, C. (2021). Aerodynamic Investigation of a Composite Low-Speed Fan for UHBR Application. J. Turbomach 143(10), 101004. https://doi.org/10.1115/1.4050671

Sanders, A. J. (2005). Nonsynchronous Vibration (NSV) due to a Flow-Induced Aerodynamic Instability in a Composite Fan Stator. J. Turbomach. 127(2), pp. 412-421. https://doi.org/10.1115/1.1811091

Stapelfeldt, S. and Brandstetter, C. (2020). Non-synchronous vibration in axial compressors: Lock-in mechanism and semi-analytical model. Journal of Sound and Vibration, Vol. 488, 8, 115649. https://doi.org/10.1016/j.jsv.2020.115649

Tateishi, A., Watanabe, T., Himeno, T., Aotsuka, M., and Murooka, T. (2016). Statistical Sensitivity Study of Frequency Mistuning on the Prediction of the Flutter Boundary in a Transonic Fan. ASME Paper GT2016-57295. https://doi.org/10.1115/GT2016-57295

Yamane, T., Yamamoto, K., Enomoto, S., Yamazaki, H., Takaki, R., and Iwamiya, T. (2001). Development of A Common CFD Platform -UPACS-. Proceedings of Parallel CFD 2000 Conference., Elsevier Science, pp. 257-264.

Zhao F., Dodds J., and Vahdati M. (2020). Influence of blade vibration on part-span rotating stall. Journal of the Global Power and Propulsion Society. 4: 285–295. https://doi.org/10.33737/jgpps/130873